Journal of Computational Physics **180,** 358–382 (2002)
doi:10.1006/jcph.2002.7099

Smoothed Particle Hydrodynamics Using Interparticle Contact Algorithms

Anatoly N. Parshikov and Stanislav A. Medin

Institute for High Energy Densities, Moscow, 125412, Russia
E-mail: parshikov@ihed.ras.ru, medin@ihed.ras.ru

Received November 15, 2000; revised May 7, 2002; published online June 19, 2002

Smoothed particle hydrodynamics (SPH) is a modern effective technique of computer simulation in continuous media mechanics. SPH approximations are quite flexible and allow various constructions. In this paper, contact interaction between particles is introduced in SPH formulation. The concept is to insert in SPH approximations of a strength medium the velocity and stresses determined at the contact point by Riemann solution, instead of mean values between velocities and stresses of basic and surrounding particles. In this case, there is no need to use artificial viscosity. In a heat-conducting medium, the contact temperature is determined by the solution of a thermal discontinuity breakup and heat fluxes in particles are computed with the use of this temperature. The modified SPH approximations easily pass various standard tests and are easily realized in multidimensional codes.

Key Words: SPH; elastic–plastic; heat conduction; discontinuity; breakup testing; numerical dissipation; 3D algorithm.

1. INTRODUCTION

Smoothed particle hydrodynamics (SPH) constitutes the meshless Lagrangian approximation which was originally introduced for computation of discontinuous flows with large deformations [1, 2]. Applied to mechanics of strength media, the SPH method proved itself to be an effective and reliable means for modeling hypervelocity impact [3–5].

Since a standard SPH method utilizes a nonconservative form of hydrodynamic equations, an artificial viscosity has to be introduced for handling oscillations around the shock front. The artificial viscosity dampens the oscillations at the shock, whereas they may be present at a contact surface.

In conservative formulation, the oscillations at the discontinuities are eliminated because fluxes of mass, momentum, and total energy, whose spatial derivatives are involved in the appropriate equations, satisfy the continuity conditions. In this case, anomalous local

0021-9991/02 $35.00

sources and sinks are not generated in the difference equations. In the difference equations the fluxes are to be computed at the boundaries of a grid cell. The Riemann solver was proposed by Godunov [6] as a rule for fluxes computation that provided the monotonicity of computational algorithms.

Referring to the conservative numerical schemes, Monaghan [7] pointed out that the dissipative terms in SPH can be constructed to be equivalent to those appearing in the Riemann formulation. He proposed that the dissipative terms in the momentum and total internal energy conservation equations were to be proportional, respectively, to the differences of velocity and total internal energy between the two particles multiplied by an effective signal velocity, which is the speed of two perturbations, one traveling from a basic particle to a surrounding particle and the other traveling in the opposite direction. The formula for the signal velocity is designed taking into account the structure of the Riemann solution. Applied to various test problems, the new SPH equations gave good results in discontinuous flow description. But in some cases, as in a problem of an impact of two streams, solution disturbances at the contact surface were observed.

Interaction between basic and surrounding particles, described by the Riemann solver, can be introduced into SPH equations directly [8, 9]. Setting a point of contact of the two particles at the line joining them, it is possible to determine an intermediate state of medium through the particle parameters by means of the Riemann solver. In [9], the intermediate values of velocity and stresses were used to replace the mean values of corresponding variables for the two contacting particles in SPH equations. In this case, there is no need to involve artificial dissipative terms.

An SPH algorithm for heat-conducting media with rapidly changing thermophysical properties was developed by Cleary and Monaghan [10]. The algorithm uses SPH approximation of divergence of heat flux and finite difference approximation of temperature gradients in the basic and surrounding particles. The temperature gradients are determined through the contact temperature of the particles, which is defined under the condition of equality of heat fluxes in the particles. This approach works ideally when the heat diffusion depth exceeds or is on the order of the dimension of the particle during the integration time step.

In this paper, an alternative method of determination of the contact temperature is considered. The contact temperature is taken from the solution of an arbitrary temperature discontinuity breakup. This approach is naturally good when the heat diffusion depth is smaller than the particle dimension during the time step.

The aim of this paper is to test these modifications of the SPH method in various problems, including elastic–plastic and heat-conducting media, to examine numerical dissipative effects and to develop a three-dimensional approximation for elastic, ideally plastic fluid.

2. SPH EQUATIONS MODIFIED WITH A RIEMANN SOLVER

Hydrodynamic Equations

First we consider ideal compressible fluid. In an SPH approximation, the continuous fluid is represented by smoothed particles. Each particle carries a mass m_i and a velocity $\vec{U_i}$ and is characterized by other specific parameters, such as a density ρ_i, a pressure P_i, and an internal energy E_i. The particle i is positioned at the point $\vec{r_i}$.

There is a variety of SPH versions of fluid dynamics equations (see [2–4]). We select as the SPH approximations of the flow equations

$$\frac{d\rho_i}{dt} = \sum_j \frac{m_j \rho_i}{\rho_j} (\vec{U_i} - \vec{U_j}) \cdot \nabla_i W_{ij}, \tag{1}$$

$$\frac{d\vec{U_i}}{dt} = -\sum_j \frac{m_j (P_i + P_j)}{\rho_j \rho_i} \nabla_i W_{ij}, \tag{2}$$

$$\frac{dE_i}{dt} = \sum_j \frac{m_j (P_i + P_j)}{2\rho_j \rho_i} (\vec{U_i} - \vec{U_j}) \cdot \nabla_i W_{ij}, \tag{3}$$

$$\frac{d\vec{r_i}}{dt} = \vec{U_i}, \tag{4}$$

where W_{ij} is the smoothing kernel (see Section 4) and the subscript j refers to the surrounding particle.

To avoid nonphysical distortions of the solution of (1)–(4), a number of measures are undertaken. Important is an introduction of the artificial dissipation terms in (2) and (3) and the artificial pressure term in (2) [11].

When the kernel W_{ij} is a function of $|\vec{r_i} - \vec{r_j}|/h$ (h being a smoothing distance), its gradient is written as

$$\nabla_i W_{ij} \left(\frac{|\vec{r_i} - \vec{r_j}|}{h} \right) = W'_{ij} \frac{\vec{r_i} - \vec{r_j}}{h|\vec{r_i} - \vec{r_j}|}. \tag{5}$$

In this case, (1)–(3) become

$$\frac{d\rho_i}{dt} = -\sum_j \frac{m_j \rho_i}{\rho_j h} W'_{ij} \left(U_i^R - U_j^R \right), \tag{6}$$

$$\frac{d\vec{U_i}}{dt} = \sum_j \frac{m_j (P_i + P_j) W'_{ij}}{\rho_j \rho_i h} \frac{\vec{r_j} - \vec{r_i}}{|\vec{r_j} - \vec{r_i}|}, \tag{7}$$

$$\frac{dE_i}{dt} = -\sum_j \frac{m_j (P_i + P_j) W'_{ij}}{2\rho_j \rho_i h} \left(U_i^R - U_j^R \right), \tag{8}$$

where

$$U^R = \vec{U} \frac{\vec{r_j} - \vec{r_i}}{h|\vec{r_j} - \vec{r_i}|}. \tag{9}$$

The structure of Eqs. (7) and (8) inspires us to suggest that each basic particle i exchanges momentum and energy with every surrounding particle j within the interaction distance $2h$. The particle interaction occurs at the contact surface element which is oriented normally to the axis R, connecting the coordinates of particles i and j, and intersects with the axis R at the point A_{ij}. In Fig. 1, the particles are drawn as spheres with the diameters D_i and D_j.

The spheres may touch ($j = 1$), may not touch ($j = 2$), and may intersect ($j = 3$). In any case, we consider the surrounding particle to be in contact with the basic one. For

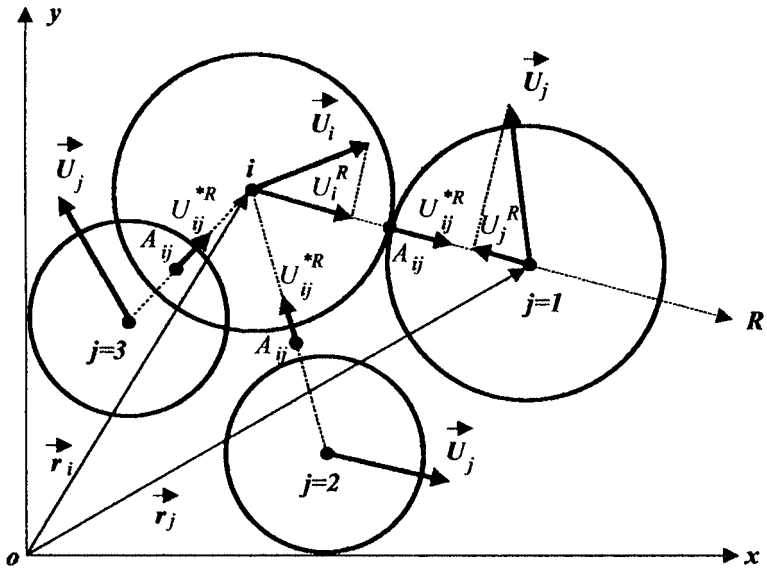

FIG. 1. Scheme of particle interaction in SPH fluid.

simplicity, the spheres in Fig. 1 are arranged in a plane that actually corresponds to 2D flow.

The position of the contact point A_{ij} at the axis R may be taken arbitrarily since the coordinates of this point do not enter the subsequent relationships.

Furthermore, the interaction of particles at A_{ij} is considered to be equivalent to that at the contact surface in continuous fluid. In this case, it is possible to determine normal velocity U_{ij}^{*R} and pressure P_{ij}^{*} at A_{ij} using the Riemann problem solution for an arbitrary discontinuity breakup. In acoustic approximation, we have

$$U_{ij}^{*R} = \frac{U_j^R \rho_j C_j + U_i^R \rho_i C_i - P_j + P_i}{\rho_j C_j + \rho_i C_i}, \tag{10}$$

$$P_{ij}^{*} = \frac{P_j \rho_i C_i + P_i \rho_j C_j - \rho_j C_j \rho_i C_i \left(U_j^R - U_i^R\right)}{\rho_j C_j + \rho_i C_i}, \tag{11}$$

where C is the sound velocity.

Transition to the modified SPH equation is realized by the substitution

$$\frac{1}{2}\left(U_i^R + U_j^R\right) \to U_{ij}^{*R} \tag{12}$$

in (6) and (8) and

$$\frac{1}{2}(P_i + P_j) \to P_{ij}^{*} \tag{13}$$

in (7). The modified SPH equations are now written as [8, 9]

$$\frac{d\rho_i}{dt} = -2\sum_j \frac{m_j \rho_i}{\rho_j h}\left(U_i^R - U_{ij}^{*R}\right) W_{ij}', \tag{14}$$

$$\frac{d\vec{U_i}}{dt} = 2\sum_j \frac{m_j P^*_{ij}}{\rho_j \rho_i h} W'_{ij} \frac{\vec{r_j} - \vec{r_i}}{|\vec{r_j} - \vec{r_i}|}, \tag{15}$$

$$\frac{dE_i}{dt} = -2\sum_j \frac{m_j P^*_{ij}}{\rho_j \rho_i h} \left(U^R_i - U^{*R}_{ij}\right) W'_{ij}. \tag{16}$$

Equations of Elastic Medium Motion

When material strength is taken into account, equations of momentum and energy conservation involve stresses. The differential equations of conservation in vector notation are written as

$$\frac{d\rho}{dt} = -\rho \nabla \cdot \vec{U}, \tag{17}$$

$$\rho \frac{d\vec{U}}{dt} = \frac{\partial \vec{\sigma^x}}{\partial x} + \frac{\partial \vec{\sigma^y}}{\partial y} + \frac{\partial \vec{\sigma^z}}{\partial z}, \tag{18}$$

$$\rho \frac{dE}{dt} = \vec{\sigma^x} \frac{\partial \vec{U}}{\partial x} + \vec{\sigma^y} \frac{\partial \vec{U}}{\partial y} + \vec{\sigma^z} \frac{\partial \vec{U}}{\partial z}, \tag{19}$$

where $\vec{\sigma^x}$, $\vec{\sigma^y}$, and $\vec{\sigma^z}$ are the stress vectors applied to surface elements orthogonal to the x, y, and z axes, respectively.

In this case, standard SPH equations of momentum and energy conservation become

$$\frac{d\vec{U_i}}{dt} = -\sum_j \frac{m_j W'_{ij}}{\rho_j \rho_i h} \left(\vec{\sigma_i^R} + \vec{\sigma_j^R}\right), \tag{20}$$

$$\frac{dE_i}{dt} = \sum_j \frac{m_j W'_{ij}}{2\rho_j \rho_i h} \left(\vec{\sigma_i^R} + \vec{\sigma_j^R}\right)\left(\vec{U_i} - \vec{U_j}\right), \tag{21}$$

where $\vec{\sigma^R}$ is a stress vector applied to a surface element, orthogonal to the axis R directed from the particle i towards the particle j (i.e., along the vector $\vec{r_j} - \vec{r_i}$, see Fig. 2),

$$\vec{\sigma^R} = [\vec{\sigma^x}(x_j - x_i) + \vec{\sigma^y}(y_j - y_i) + \vec{\sigma^z}(z_j - z_i)] \frac{1}{|\vec{r_j} - \vec{r_i}|}. \tag{22}$$

For determination of intermediate values of medium variables resulting from the particles' contact discontinuity breakup, we introduce the coordinate system RST. The axes S and T are located in the contact surface (the plane abc in Fig. 2), the axis S being in the plane zoR. The initial discontinuity is set up in the coordinate system RST as a plane contact surface separating two regions with uniform quantities $\vec{U_i}$, ρ_i, and $\vec{\sigma_i^R}$ at the left side and $\vec{U_j}$, ρ_j, and $\vec{\sigma_j^R}$ at the right side. This discontinuity breaks up into two waves, longitudinal and tangential, both traveling to the left and to the right directions along the axis R. The velocity $\vec{U^*_{ij}}$ and the stress vector $\vec{\sigma^{*R}_{ij}}$ at the contact surface (point A_{ij}) are determined by

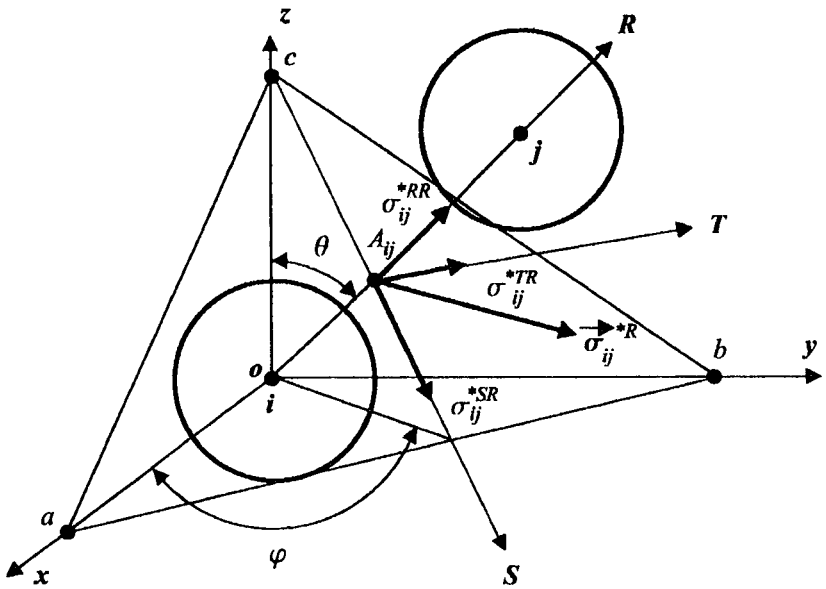

FIG. 2. Coordinate system *RTS* and stresses at the contact surface *abc*.

the Riemann solver. In acoustic approximation, we have for the longitudinal wave

$$U_{ij}^{*R} = \frac{U_j^R \rho_j C_j^l + U_i^R \rho_i C_i^l + \sigma_j^{RR} - \sigma_i^{RR}}{\rho_i C_i^l + \rho_j C_j^l}, \tag{23}$$

$$\sigma_{ij}^{*RR} = \frac{\sigma_j^{RR} \rho_i C_i^l + \sigma_i^{RR} \rho_j C_j^l + \rho_i C_i^l \rho_j C_j^l \left(U_j^R - U_i^R\right)}{\rho_i C_i^l + \rho_j C_j^l}, \tag{24}$$

and for the tangential wave

$$U_{ij}^{*S} = \frac{U_j^S \rho_j C_j^t + U_i^S \rho_i C_i^t + \sigma_j^{SR} - \sigma_i^{SR}}{\rho_i C_i^t + \rho_j C_j^t}, \tag{25}$$

$$\sigma_{ij}^{*SR} = \frac{\sigma_j^{SR} \rho_i C_i^t + \sigma_i^{S} \rho_j C_j^t + \rho_i C_i^t \rho_j C_j^t \left(U_j^S - U_i^S\right)}{\rho_i C_i^t + \rho_j C_j^t}, \tag{26}$$

$$U_{ij}^{*T} = \frac{U_j^T \rho_j C_j^t + U_i^T \rho_i C_i^t + \sigma_j^{TR} - \sigma_i^{TR}}{\rho_i C_i^t + \rho_j C_j^t}, \tag{27}$$

$$\sigma_{ij}^{*TR} = \frac{\sigma_j^{TR} \rho_i C_i^t + \sigma_i^{TR} \rho_j C_j^t + \rho_i C_i^t \rho_j C_j^t \left(U_j^T - U_i^T\right)}{\rho_i C_i^t + \rho_j C_j^t}, \tag{28}$$

where C^l and C^t are the velocities of longitudinal and transversal waves in a medium, respectively.

In (23)–(28), all quantities are calculated with respect to the coordinate system RST, i.e., $\vec{U} = U^R \vec{e^R} + U^S \vec{e^S} + U^T \vec{e^T}$ and $\vec{\sigma^R} = \sigma^{RR} \vec{e^R} + \sigma^{SR} \vec{e^S} + \sigma^{TR} \vec{e^T}$. The formulae of a quantity transformation from the frame xyz to the frame RST and the reverse are given in Appendix B. Now the standard equations of motion (20) and energy (21) can be modified

by substitution,

$$\frac{1}{2}(\overrightarrow{U_i} + \overrightarrow{U_j}) \to \overrightarrow{U_{ij}^*} \tag{29}$$

and

$$\frac{1}{2}(\overrightarrow{\sigma_i^R} + \overrightarrow{\sigma_j^R}) \to \overrightarrow{\sigma_{ij}^{*R}}. \tag{30}$$

In (29) and (30), the vectors $\overrightarrow{U_{ij}^*}$ and $\overrightarrow{\sigma_{ij}^{R*}}$ are calculated in the coordinate system xyz and have to be recomputed in terms of quantities (23)–(28). This is done in Appendix B.

As a result, the modified SPH equations of momentum and energy conservation come to

$$\frac{d\overrightarrow{U_i}}{dt} = -\sum_j \frac{2m_j W'_{ij}}{\rho_j \rho_i h} \overrightarrow{\sigma_{ij}^{*R}}, \tag{31}$$

$$\frac{dE_i}{dt} = \sum_j \frac{2m_j W'_{ij}}{\rho_j \rho_i h} \overrightarrow{\sigma_{ij}^{*R}} (\overrightarrow{U_i} - \overrightarrow{U_{ij}^*}). \tag{32}$$

The equation of mass conservation is presented by (14).

The equations of conservation should be supplied with constitutive equations. The equations for elastic, ideally plastic media, and their SPH approximations when needed, are presented below and in Appendix A.

3. HEAT CONDUCTION SPH EQUATIONS

Fast Heat Diffusion

The energy equation limited only by accounts of heat conduction is

$$\rho \frac{dE}{dt} = -div\, \vec{q}, \tag{33}$$

where $\vec{q}$ is the heat flux vector. The SPH approximation of (33) is written as

$$\frac{dE_i}{dt} = \sum_j \frac{m_j W'_{ij}}{\rho_j \rho_i h} (q_i^R + q_j^R), \tag{34}$$

where

$$q^R = \vec{q} \frac{\overrightarrow{r_j} - \overrightarrow{r_i}}{|\overrightarrow{r_j} - \overrightarrow{r_i}|}.$$

The Fourier's law SPH approximation could close the energy equation (34). As a better approach, discussed in [10], finite differences are used in the following analysis.

For calculation of q_i^R and q_j^R, Cleary and Monaghan [10] proposed the procedure using the contact temperature T_{ij}^* of basic and surrounding particles. According to that, we have

$$q_i^R = -\lambda_i \frac{T_{ij}^* - T_i}{\Delta r_i}, \tag{35}$$

$$q_j^R = -\lambda_j \frac{T_j - T_{ij}^*}{\Delta r_j}, \tag{36}$$

where λ is the heat conductivity.

The contact temperature T_{ij}^* and Δr_i and Δr_j are defined by Cleary and Monaghan [10] under conditions

$$q_i^R = q_j^R, \tag{37}$$

$$\Delta r_i = \Delta r_j = \frac{1}{2}|\vec{r_j} - \vec{r_i}|. \tag{38}$$

In this case, T_{ij}^* is found as

$$T_{ij}^* = \frac{\lambda_i T_i + \lambda_j T_j}{\lambda_i + \lambda_j}. \tag{39}$$

Finally, we come to the Cleary and Monaghan [10] SPH heat conduction equation [10]

$$\frac{dE_i}{dt} = -\sum_j \frac{m_j W_{ij}'}{\rho_j \rho_i h} \frac{4\lambda_i \lambda_j}{\lambda_i + \lambda_j}(T_j - T_i)\frac{1}{|\vec{r_j} - \vec{r_i}|}. \tag{40}$$

This equation has been successfully tested for various analytical solutions including multiple materials with substantially different conductivities and specific heats [10].

Referring to the conditions (37) and (38), one can conclude a priori that Eq. (40) would work perfectly when heat diffusion is accomplished at the smoothing distance h during the time step Δt^n, which is expressed by the condition [10]

$$\Delta t^n = \beta \rho C_V h^2/\lambda, \tag{41}$$

where C_V is the specific heat capacity. The integration proved to be stable, in various tests [10], if $\beta \leq 0.15$.

Slow Heat Diffusion

When the heat diffusion is not fast enough, so that the diffusion depth (skin layer) does not exceed the smoothing distance, it is better to define the contact temperature T_{ij}^* in terms of transient heat transfer between basic and surrounding particles. This process is described by the solution of the problem of temperature discontinuity breakup. The one-dimensional Fourier equation with discontinuous at $x = 0$ thermophysical properties is solved for initial conditions $T(x, 0) = T_i$, $x < 0$ and $T(x, 0) = T_j$, $x > 0$. The temperature distribution is given by [12]

$$T - T_{ij}^* = \begin{cases} (T_{ij}^* - T_i) erf\frac{x}{2\sqrt{a_i t}}, & \text{for } x < 0, \\ (T_j - T_{ij}^*) erf\frac{x}{2\sqrt{a_j t}}, & \text{for } x > 0, \end{cases} \tag{42}$$

where T_{ij}^* is the contact temperature at $x = 0$,

$$T_{ij}^* = \frac{\lambda_i T_i + \lambda_j T_j \sqrt{a_i/a_j}}{\lambda_i + \lambda_j \sqrt{a_i/a_j}}, \tag{43}$$

and

$$a = \frac{\lambda}{\rho C_V} \tag{44}$$

is the thermal diffusivity.

The characteristic distances in heat fluxes (35) and (36) are proportional to thermal skin layers in the particles i and j. Their magnitudes vary in time. The limiting values of Δr_i and Δr_j providing stability of integration satisfy the following condition:

$$\Delta r_i + \Delta r_j = |\vec{r_i} - \vec{r_j}|, \quad \Delta r_i / \Delta r_j = \sqrt{a_i/a_j}. \tag{45}$$

When the condition $\Delta r_i + \Delta r_j \le |\vec{r_i} - \vec{r_j}|$ takes place, an increased numerical diffusion occurs at the same time step.

Combining (43) and (45) with (34)–(37), we obtain the SPH heat conduction equation in the form

$$\frac{dE_i}{dt} = -\sum_j \frac{m_j W'_{ij}}{\rho_j \rho_i h} 2\lambda_i \lambda_j \frac{1 + \sqrt{a_i/a_j}}{\lambda_i + \lambda_j \sqrt{a_i/a_j}} (T_j - T_i) \frac{1}{|\vec{r_j} - \vec{r_i}|}. \tag{46}$$

When the thermal diffusivities of particles i and j are equal, Eqs. (46) and (40) coincide, as the contact temperatures in (43) and (45) are equal as well.

4. 1D NUMERICAL TESTS

In tests, we use the cubic spline kernel [4]

$$W_{ij} = \begin{cases} (1 - 1.5\phi^2 + 0.75\phi^3)/N & \text{for } 0 \le \phi < 1 \\ 0.25(2 - \phi)^3/N & \text{for } 1 \le \phi < 2, \\ 0 & \text{for } 2 \le \phi \end{cases} \tag{47}$$

where $\phi = |\vec{x_i} - \vec{x_j}|/h$, $N = 1.5h$ for 1D flow, $N = 0.7\pi h^2$ for 2D flow, and $N = \pi h^3$ for 3D flow. The smoothing distance h is calculated according to [3] as

$$h = 0.5(D_i + D_j), \tag{48}$$

where $D = m/\rho$ for a 1D problem.

Riemann Problem in Perfect Gas

The equation of state is

$$P = (\gamma - 1)\rho E. \tag{49}$$

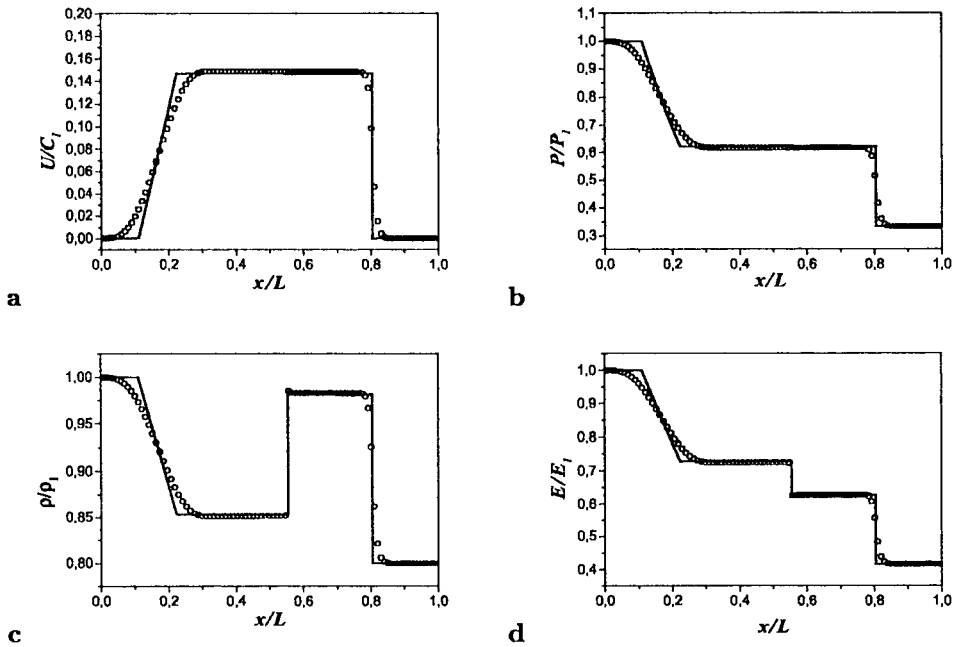

FIG. 3. Solution of Riemann problem in a perfect gas. Velocity (a), pressure (b), density (c), and specific energy (d) against distance. Solid line presents analytical solution.

The discontinuity is initially set up at $x/L = 0.5$ (L being the computational interval) by pressure and density jumps. The values of the quantities are $P_1 = 3 \times 10^4$ Pa, $P_2 = 1 \times 10^4$ Pa, $\rho_1 = 1.5 \times 10^3$ kg/m^3, $\rho_2 = 1.2 \times 10^3$ kg/m^3, and $U_1 = U_2 = 0$. The specific heat ratio is $\gamma_1 = \gamma_2 = 3$. The computational interval is $L = 0.1$ m and contains 200 particles.

In Fig. 3, the analytical and numerical solutions are drawn for dimensionless velocity, pressure, density, and energy, at the time 0.004 s. The solid line corresponds to the analytical solution. The shock and the contact surface are simulated well. The rarefaction wave is rather stretched.

Riemann Problem in Elastic, Perfectly Plastic Matter

The equation of state is taken as

$$P = K(\rho - \rho_0)/\rho_0, \tag{50}$$

where $K = const$ is the isothermal bulk modulus.

Following the Wilkins methodology [18] for the condition of uniaxial strain, the deviatoric stress S_{xx} is computed from the strain rate

$$\frac{dS^{xx}}{dt} = 2G\frac{de^{xx}}{dt}. \tag{51}$$

The SPH approximation of the strain rate is

$$\frac{de_i^{xx}}{dt} = -\frac{4}{3}\sum_j \frac{m_j W'_{ij}}{\rho_i h}\left(U_{ij}^{*x} - U_i^x\right), \tag{52}$$

where U_{ij}^{*x} is determined by formula (23) with superscript R changed to x.

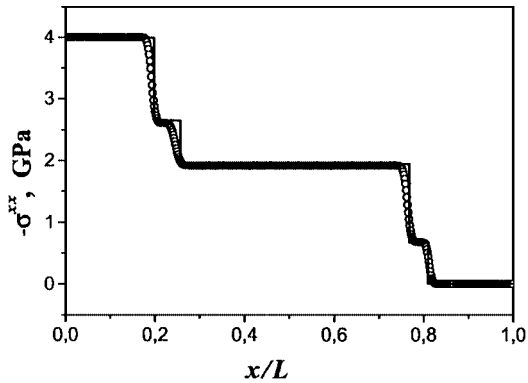

FIG. 4. Solution of Riemann problem in elastic, perfectly plastic medium. Normal stress against distance. Solid line presents analytical solution.

At plastic flow submitted to the von Mises criterion, the computed value of S^{xx} is corrected by factor $2Y_0/3S^{xx}$.

The initial discontinuity at $x/L = 0.5$ is set up as $\sigma_1^{xx} = 4$ GPa, $\sigma_2^{xx} = 0$, $\rho_1 = \rho_2 = 2700$ kg/m^3.

The properties of aluminum are the following: $K = 73$ GPa, $G = 23$ GPa, and $Y_0 = 0.3$ GPa.

The length of the computational interval is 0.1 m; the number of particles is 200. In Fig. 4, the results of computations are presented at the time 5 μs. The solid line is the analytical solution. It is seen that the numerical solution does well at maintaining the amplitude and velocities of elastic and plastic waves.

Heat Conduction

The solution of temperature discontinuity breakup (42) is used for testing the SPH approximation (46). This test was proposed by Cleary and Monaghan [10] and successfully applied to the approximation (40).

The computational segment of 0.1 m is composed of two different materials contacting each other at $x/L = 0.5$. The thermophysical properties of material are given in Table I. The number of particles is 100. The initial conditions are $T(x, 0) = 300$ K, $x/L < 0.5$, and $T(x, 0) = 1000$ K, $x/L > 0.5$. At the segment boundaries, the condition of zero heat flux is fixed, and at the contact point, the continuity of temperature and heat fluxes is kept up. Four pairs of materials were considered: aluminum–aluminum, aluminum–brass, aluminum–lead, and aluminum–china. The results of the computations are plotted in Fig. 5.

There is satisfactory agreement between the numerical (circles) and analytical (solid curves) solutions. When two different materials are coming into contact, the contact

TABLE I
Thermophysical Properties of Materials

Material	Aluminum	Brass	Lead	China	Gas
ρ_0, kg/m^3	2,700	8,700	11,350	2,500	3.75×10^{-3}
C_v, $J/(\mathrm{kg} \cdot \mathrm{K})$	880	380	130	920	5.2×10^3
λ, $W/(\mathrm{m} \cdot \mathrm{K})$	209	85.5	35	1.68	2.3

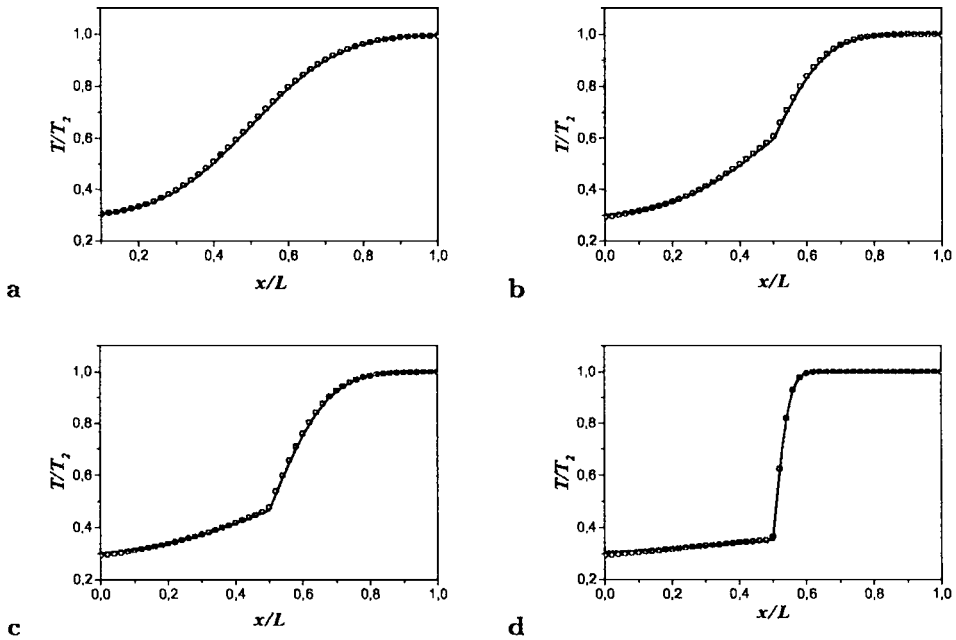

FIG. 5. Temperature profiles after temperature discontinuity breakup for (a) aluminum–aluminum at time $t = 2$ s, (b) aluminum–brass at time $t = 3$ s, (c) aluminum–lead at time $t = 4$ s, and (d) aluminum–china at time $t = 10$ s.

temperature follows (43) and the shape of the curve's left and right branches corresponds to the values of thermal diffusivity of the material (thermal skin layer).

The computations presented in Fig. 5 were performed for Eq. (46). Equation (40) for all four cases has fully identical results (the difference in computations cannot be distinguished graphically). Cleary and Monaghan note [10] that for ratios of thermal diffusivity up to 1000 : 1, Eq. (40) provides good accuracy. The discrepancy might be expected at very high ratios a_1/a_2. To illustrate this, the thermal contact of china and gas was computed. The material data for this pair are given in Table I. The temperature profiles decribed by Eqs. (40) and (46) at time 4×10^{-9} s ($L = 10^{-4}$ m) are plotted in Fig. 6. The contact point

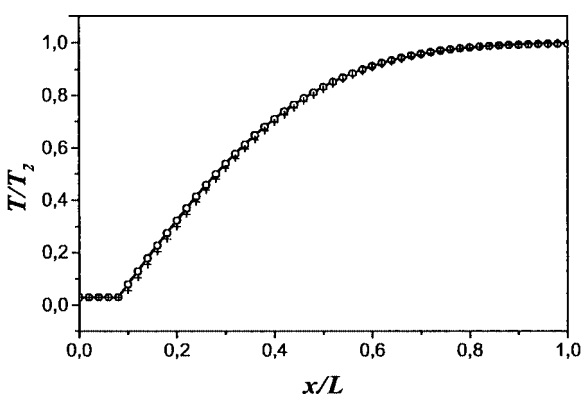

FIG. 6. Temperature profiles after temperature discontinuity breakup for china–gas, computed according to Eqs. (40) (+) and (46) (○). The solid line is the analytical solution.

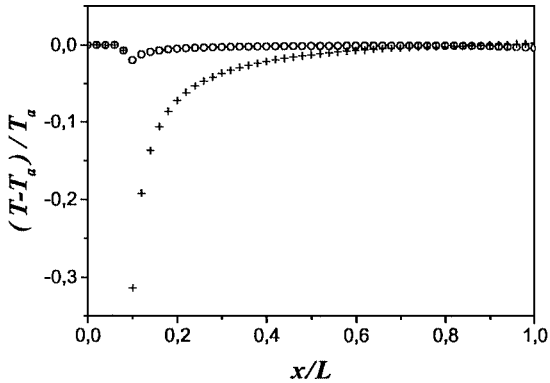

FIG. 7. Relative error of temperature computation according to Eqs. (40) (+) and (46) (○). T_a is the analytical solution.

is set up at $x/L = 0.1$. In Fig. 7, the relative errors of temperature computation according to Eqs. (40) and (46) are drawn. Equation (40) gives the maximum error of -0.35 for gas temperature near the contact point. It should be noted that in this computation the ratio of thermal diffusivities is taken to be very high, i.e., 2×10^9.

Experience with computations of the modified SPH equations shows that integration is stable for values of β (41) up to 0.35.

Blast Wave

Since the blast wave results in an extremely severe change of gas parameters, the acoustic approximation (10)–(11) of the Riemann solver must be replaced by the exact solution of the discontinuity breakup. For computation of the intermediate values of velocity U_{ij}^{*R} and pressure P_{ij}^{*}, a noniterative Riemann solver [13] was used.

The discontinuity is initially located at $x/L = 0.5$, and values of gas parameters are $P_1 = 30\,\text{GPa}$, $P_2 = 0.1\,\text{MPa}$, $\rho_1 = \rho_2 = 1.0\ \text{kg/m}^3$, and $U_1 = U_2 = 0$. The equation of state is taken for an ideal gas (49) with the specific heat ratios $\gamma_1 = 1.3$ and $\gamma_2 = 1.4$. The computational interval $L = 0.1$ m contains 200 particles.

The numerical solution is presented in Fig. 8. This is the best case obtained when the factor 2 in the continuity equation (14) was changed to 1.75. The analytical solution is shown by the solid line. In the case when the factor 2 is kept, the density in the compression spike is rather underestimated. There are visible distortions of gas parameter distributions in both expansion and compression parts of the flow.

In Fig. 9, the solution of the standard equation (6)–(9), in which artifical viscosity terms according to friction momentum flux density

$$\pi_i = 20\rho_i D_i^2 \dot{\varepsilon}_i |\dot{\varepsilon}_i| + 0.5\rho_i D_i C_i \dot{\varepsilon}_i \tag{53}$$

are involved, is plotted. The computations were performed using the algorithm described in Appendix B. It is seen that there are oscillations around the contact interface. The computational work in this case was increased by factor of 7. Some additional measures are to be taken in order to suppress these oscillations. Substantial dumping of oscillations occurs

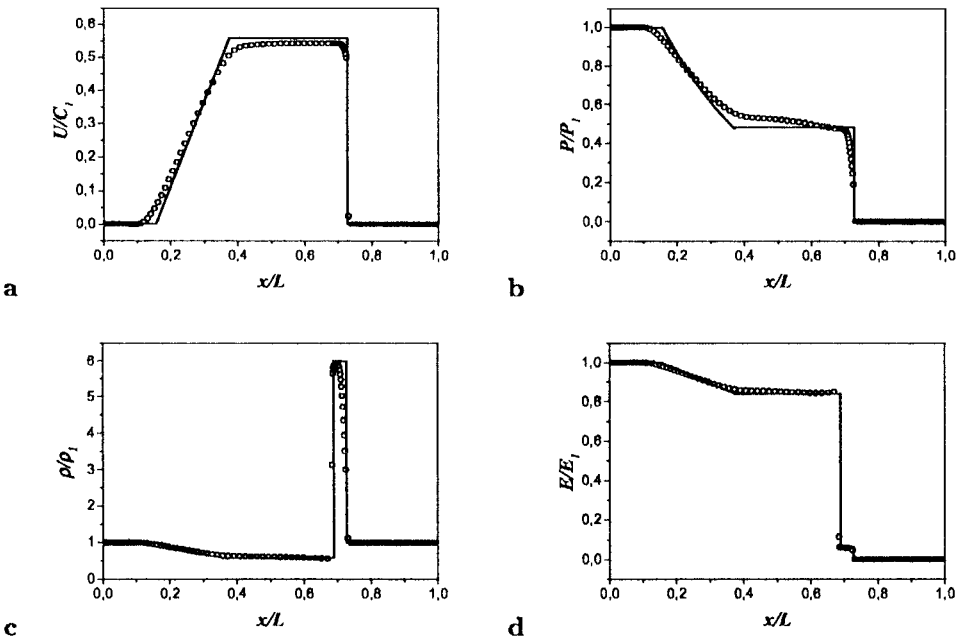

FIG. 8. Solution for the blast wave in a perfect gas computed by the modified SPH.

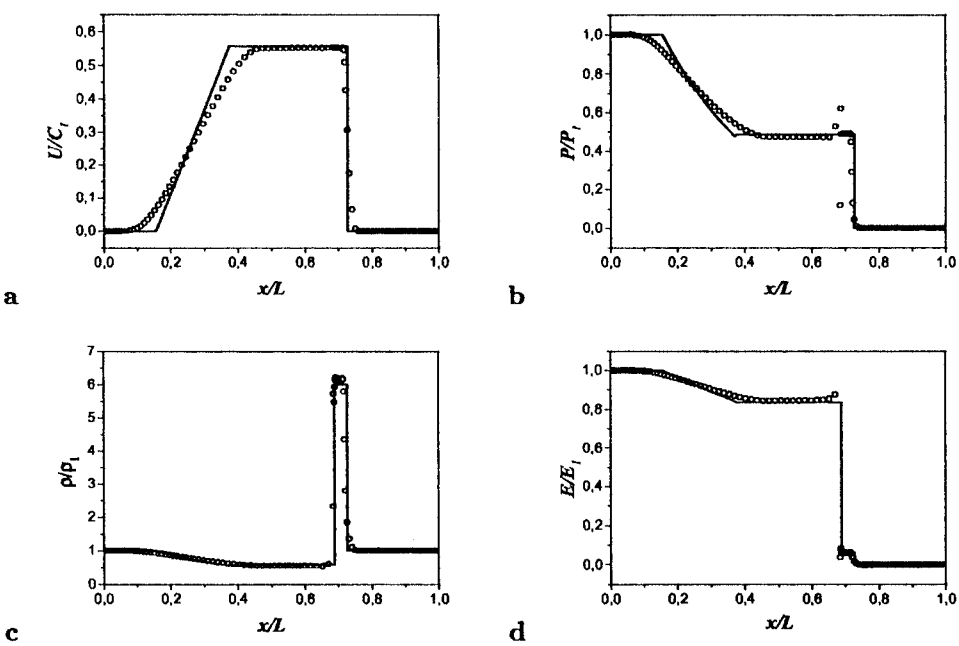

FIG. 9. Solution for the blast wave in a perfect gas computed by the standard SPH with artificial viscosity (53).

when the energy equation is written and approximated in terms of total internal energy $E + 0.5U^2$ [7].

5. 2D TEST COMPUTATIONS

In this section, 2D computations are presented with the aim of examining the dissipative numerical effects in the modified SPH algorithm. The stability of the flow with respect to unwanted numerical fragmentation is also touched on.

The Impact of Rubber Cylinders

The formulation of this problem is taken from [11]. Two rubber cylinders impact each other along a generatrix located at the line connecting the centers of the cylinders (normal impact). The initial data were specified as follows: the external radius is 0.0425 m, the internal radius is 0.0275 m, the density $\rho_0 = 1.2 \times 10^3$ kg/m^3, shear modulus $G = 0.22$ MPa, and the sound velocity $C_0 = 850$ m/s, which is involved in the equation of state

$$P = (\rho - \rho_0)C_0^2. \tag{54}$$

Before the impact, each cylinder has velocity 50 m/s. Each cylinder consists of three rows of particles with a total of 135. The results of computations are presented in Fig. 10. Figures 10a to 10f show times $t = 0$, 0.5, 2, 5, 10, and 18 ms, respectively. At the impact, the cylinders are compressed without fracturing. Then they bounce off each other. The subsequent oscillations are sharply dumped, limited by only one intensive pulsation. This can be attributed to the large numerical viscosity of the algorithm. The increase of particles to 1080 did not lead to the cylinder fracture.

Problem of Two Half-Spaces with Zero Physical Viscosity

This test is aimed at demonstration of numerical viscosity of the modified SPH algorithm. The formulation of the problem is analogous to that of the first Stokes problem. Two half-spaces that are in contact and initially at rest are suddenly caused to move along the contact surface with a velocity U_0^x in opposite directions. To observe the only numerical shear viscosity the liquid is supposed to be nonviscous. 2D flow takes place in the x, y plane. The x axis is the contact line. The equation of state is taken in the form of (54), where $\rho_0 = 2.7 \times 10^3$ kg/m^3 and $C_0 = 5.2 \times 10^3$ kg/m^3 are the properties of aluminum and $G = 0$ ($Y_0 = 0$) for liquid fluid. The dimensions of the computational region are presented in Fig. 11. There are 20×20 particles of 3.85×10^{-3} m diameter. The velocity U_0^x is equal to 250 m/s.

The evolution of computed flow is shown in Fig. 11. At the initial moment the particles at $y > 0$ move to the right with a velocity of 250 m/s, the particles at $y < 0$ move in the opposite direction with the same velocity. The heavy curve crossing the coordinate origin represents the displacement of particles. In case of zero numerical viscosity, this curve should be piecewise constant with the discontinuity at $y = 0$. The numerical diffusion makes the curve continuous. The displacement of particles resembles the real displacement in viscous flow [14], decribed by (42), where substitution $x \Rightarrow y$, $\lambda_i = \lambda_j$, and $a_i = a_j = \nu$, $T_i = -T_j = U_0^x$

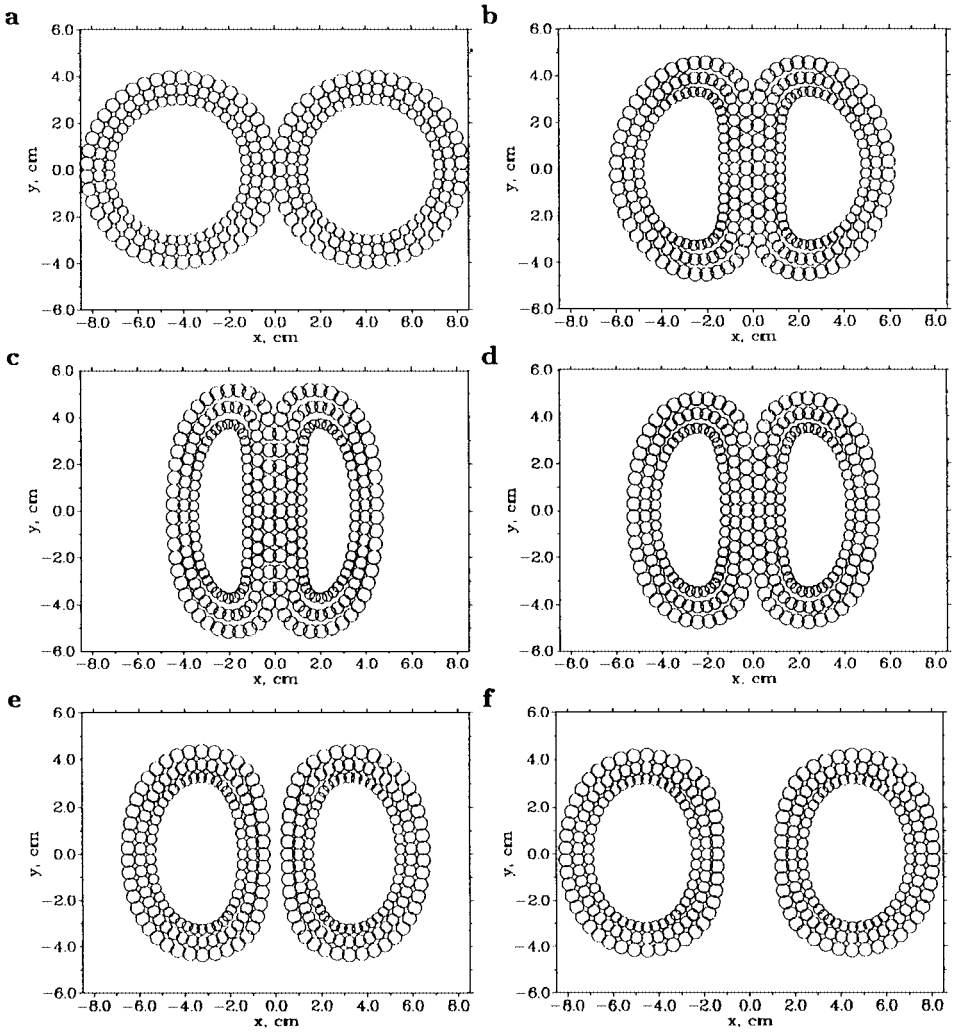

FIG. 10. Rubber cylinders impacting and bouncing. The phases of compression and expansion are shown at times (a) 0, (b) 0.5, (c) 2, (d) 5, (e) 10, and (f) 18 ms.

is to be made. Conforming the analytical solution (42) to the curve of Fig. 11 gives an evaluation of numerical shear viscosity in terms of numerical kinematic viscosity ν_{num}. In this particular case, $\nu_{num} = 7$ m^2/s.

When the artificial viscosity is introduced in standard SPH it is possible to compare numerical and artificial viscosities. If the artificial momentum flux density is defined as $\pi^{xy}_{art} \sim \alpha \rho_i C^t_i |\overrightarrow{U_i} - \overrightarrow{U_j}|$ and numerical shear stress is evaluated as $\pi^{xy}_{num} \sim \rho_i \nu_{num} |\overrightarrow{U_i} - \overrightarrow{U_j}|/D_i$, the ratio of numerical and artificial viscosities is $\pi^{xy}_{num}/\pi^{xy}_{art} \sim \nu_{num}/\alpha C^t_i D_i$. For $\alpha = 1$ and $C^t = 2.9 \times 10^3$ m/s, the viscosity ratio is $\pi^{xy}_{num}/\pi^{xy}_{art} \sim 0.63$.

In computation of shear waves the numerical viscosity causes spreading of a discontinuous front. The physical viscous spreading of the shear discontinuity is evaluated as $\delta \sim \nu/C^t$. The numerical spreading $\delta_{num}/D_i \sim \nu_{num}/C^t D_i$ for the present conditions is on the order of one particle.

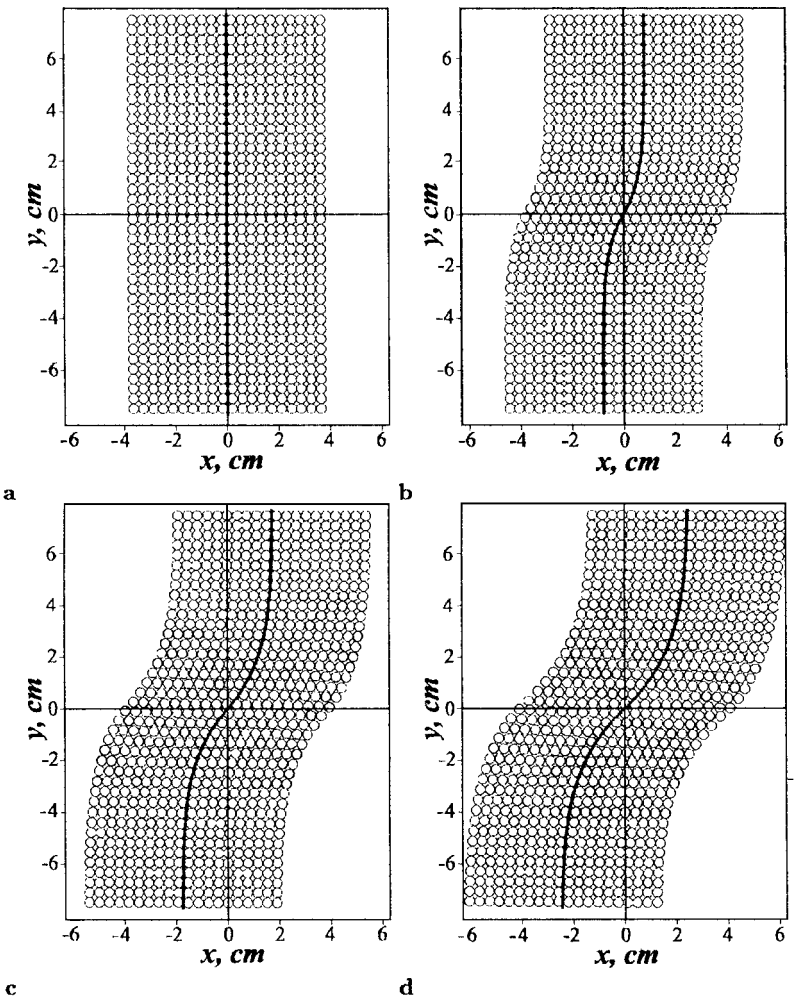

FIG. 11. Flow of nonviscous fluid with initial tangential discontinuity of velocity. The initial position of the particles (a) and their displacement at the times (b) 32, (c) 70, and (d) 99 μs. The heavy curve, corresponding to Eq. (42), shows the displacement of particles originally positioned at $x = 0$.

Rotation of an Elastic Plate

An elastic disc plate with a 10-cm radius rotates around the axis crossing its center and normal to its plane. The plate consists of aluminum particles each with diameter 2.55×10^{-3} m. The elastic properties of aluminum are given in the previous section (see elastic perfectly plastic test). Yield stress is $Y_0 = \infty$. The plate is considered to be thin and the stress vector $\overrightarrow{\sigma^z}$ (22) is equal to zero.

The computations are performed for the following initial conditions: the disc rotates with an angular velocity $\Omega = 3 \times 10^3$ s^{-1}; the stresses are given by the analytical solution [15].

Figure 12 presents the material distribution at various times $t =$ (a) 0, (b) 0.33, (c) 0.65, and (d) 1.74 ms. At the times (b) to (d), the rotation angle amounts to $\pi/4$, $\pi/2$, and $2\pi/3$, and the angular momentum decreases as $L_z/L_0 = 0.64$, 0.26, and 0.017, correspondingly.

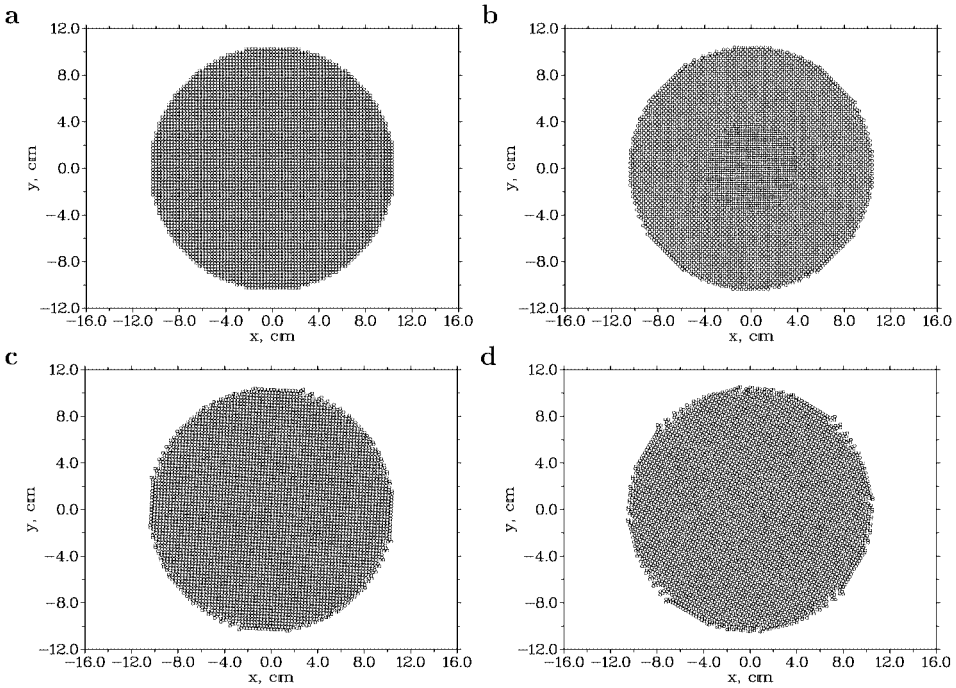

FIG. 12. Material distribution in a rotating disc plate at $t =$ (a) 0, (b) 0.33, (c) 0.65, and (d) 1.74 ms.

6. 3D IMPACT SIMULATION

SPH is a convenient and effective method for programming multidimensional equations. At the moment, there are a number of studies on 3D simulation using SPH [16, 17]. The 3D algorithm of modified SPH equations for an elastic, perfectly plastic medium is described in Appendix B. In this section, the impact of a steel cube against a steel plate at different angles between the projectile trajectory and the target normal is considered.

The projectile cube approaches the target plate with its front face parallel to the plate. The surfaces of contacting materials are supposed to be absolutely smooth, i.e., tangential stresses at the material interface are absent:

$$\sigma_{ij}^{*SR} = \sigma_{ij}^{*TR} = 0. \tag{55}$$

The material properties for the projectile cube are $K_1 = 176$ GPa, $G_1 = 83$ GPa, $\rho_1 = 7900\,\text{kg/m}^3$, $\gamma_1 = 2$, and $Y_{01} = 0.5$ GPa, and for the target plate $K_2 = 176$ GPa, $G_2 = 83$ GPa, $\rho_2 = 7900\,\text{kg/m}^3$, $\gamma_2 = 2$, and $Y_{02} = 1.9$ GPa. The cube size is equal to 0.01 m; the dimensions of the plate are $0.005 \times 0.0667 \times 0.0667$ m^3. The number of particles is $6 \times 6 \times 6$ for the projectile and $3 \times 40 \times 40$ for the target. The absolute velocity of the cube is 2000 m/s. The plate thickness and the projectile velocity are selected to simulate a wide range of impact events from normal perforation to oblique ricochet. Figure 13 shows normal impact. The projectile particles are shown as black spheres; the target particles are shown as open spheres. Figure 13 shows a typical scenario of impact of strength materials, demonstrating perforation with plastic deformation of the projectile and plug formation of the target

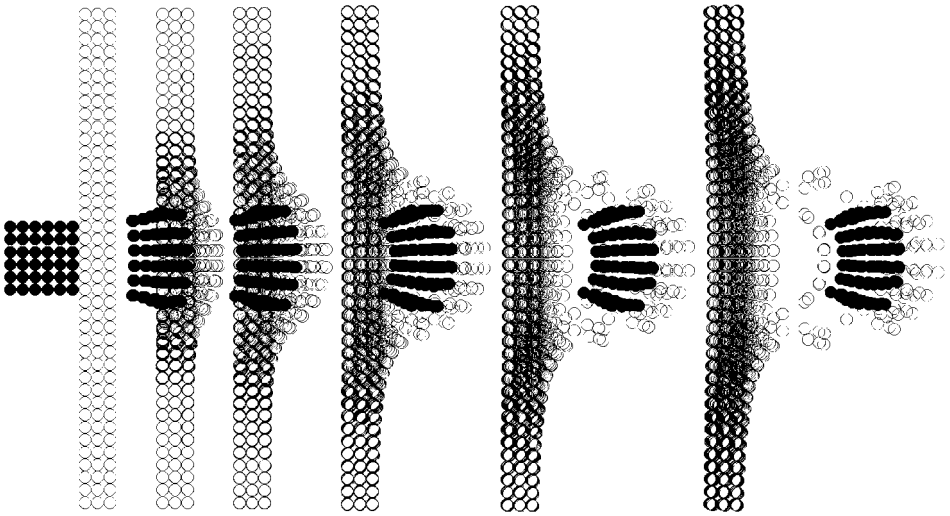

FIG. 13. Computed evolution of material during normal impact of a steel cube on a steel plate. The phases of the impact are fixed at the times 0, 10, 20, 40, 60, and 80 μs, successively.

material. At the back face of the plate, the material flows over the edges, forming four tongues along the cube normal faces.

The oblique impact of an angle of 30° is shown in Fig. 14. In this case, the projectile deformation is more severe and more target material is involved in the flow.

The ricocheting impact occurs at an obliquity angle of 80° (see Fig. 15). Computations show elastoplastic deformations of the materials. The projectile bounces off the target plate. The propagation of a compression wave is observed in the target plate.

The presented results demonstrate adequate performance of a 3D SPH simulation of elastoplastic flows based on the interparticle contact algorithm.

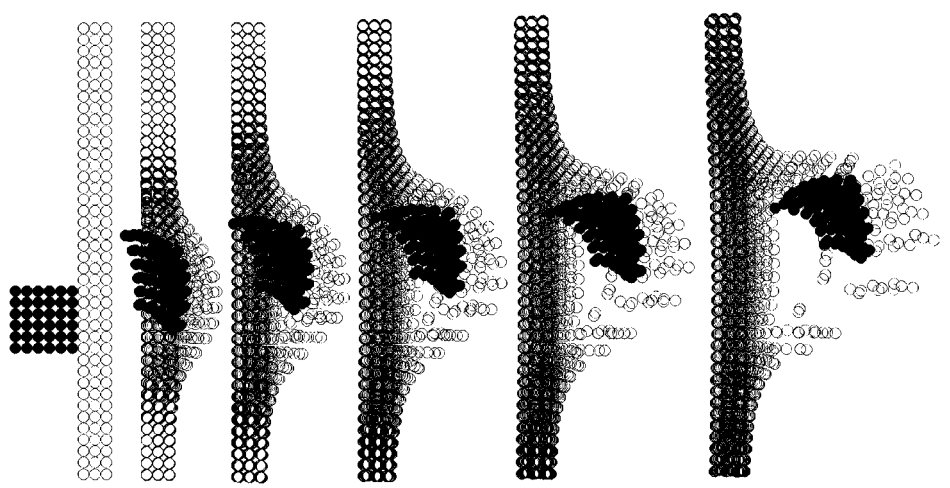

FIG. 14. Computed evolution of material during a steel cube oblique impact on a steel plate. The obliquity angle is 30°. The phases of the impact are fixed at the times 0, 20, 40, 60, 80, and 120 μs, successively.

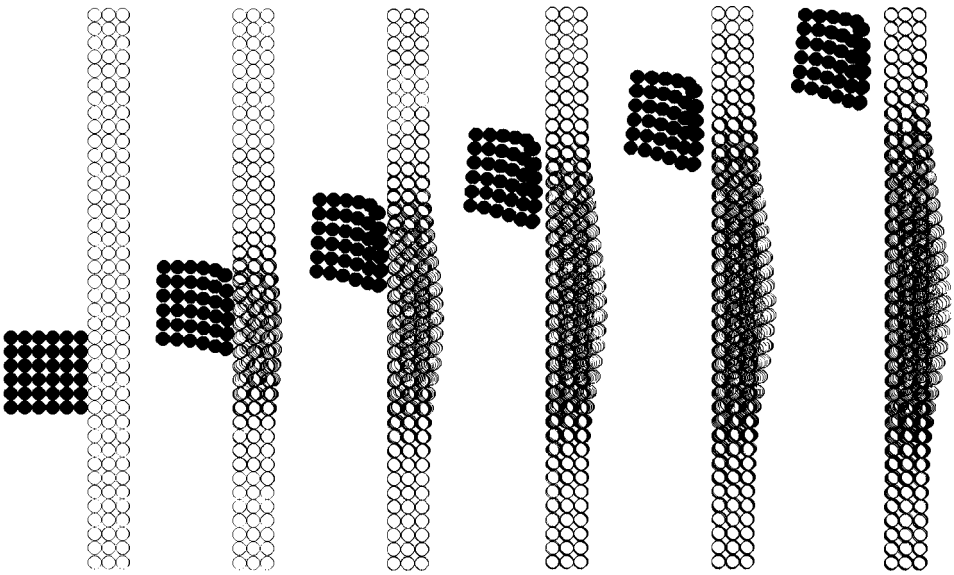

FIG. 15. Computed evolution of material during the ricocheting impact of a steel cube on a steel plate. The obliquity angle is 80°. The phases of the impact are fixed at the times 0, 10, 20, 30, 40, and 50 μs, successively.

7. SUMMARY

In SPH media, the basic and surrounding particles are interacting along the line connecting their centers. Supposing that the particles touch each other at some virtual point of this line, one can determine the intermediate parameters at this point. The velocity and the stress vector applied to the surface element normal to the connecting line are given by the Riemann solver. The intermediate values are inserted in the SPH equation instead of the mean values of velocity and the stress vector.

The intermediate temperature is found from the solution of a thermal discontinuity breakup. This solution suggests an evolution of finite difference approximations of heat fluxes at the interface of the basic and surrounding particles. To keep the numerical diffusion as low as possible, under the condition that the integration is stable, the sum of skin thermal layers in the particles pair at the time step is taken to be equal to the interparticle distance. This condition determines the structure of the SPH Fourier equation.

Comparison of the solutions of the two-material thermal contact problem given by the modified SPH Fourier equation with those of Cleary and Monaghan [10] shows that the modified algorithm provides better accuracy at very high ratios of thermal diffusivity.

The SPH approximations modified with the use of discontinuity breakup solutions satisfy various tests. In standards tests of discontinuity breakup in perfect gas, elastic plastic, and thermal conduction media, the proposed algorithms work well.

In more severe tests, such as blast wave, bouncing of rubber cylinders, shear flow, and rotation, the modified SPH, technique discloses rather high numerical viscosity. This is the major concern for further development of this technique.

In multidimensional algorithms for strength media, the stress transformations from the computational frames of reference to the frame at the interparticle interface and the reverse are used for computation of the intermediate parameters. This can be accomplished by

standard software, and stress transformations in the stress deviator corrections can account for the rigid body rotation. The three-dimensional version of the SPH elastic, ideally plastic algorithm demonstrates effective and stable performance.

APPENDIX A

Constitutive Equations and Equation of State

The stress tensor is composed of an isotropic part (pressure) and a deviatoric stress tensor

$$\sigma^{\alpha\beta} = -P\delta^{\alpha\beta} + S^{\alpha\beta}. \tag{A.1}$$

The elastic deviatoric stress tensor is determined by the constitutive equation

$$\frac{dS_e^{\alpha\beta}}{dt} = 2G\frac{de^{\alpha\beta}}{dt}, \tag{A.2}$$

where G is the shear stress modulus.

The deviatoric strain rate tensor is defined as

$$\frac{de^{\alpha\beta}}{dt} = \frac{1}{2}\left(\frac{\partial U^\alpha}{\partial x^\beta} + \frac{\partial U^\beta}{\partial x^\alpha}\right) - \frac{1}{3}\delta^{\alpha\beta}\frac{\partial U^\gamma}{\partial x^\gamma}. \tag{A.3}$$

The SPH approximation of (A.2) taking into account (A.3) is

$$\frac{dS_{ei}^{\alpha\beta}}{dt} = 2G\sum_j \frac{m_j W'_{ij}}{\rho_j h}\left[\left(U_i^\alpha - U_{ij}^{*\alpha}\right)\left(x_j^\beta - x_i^\beta\right) + \left(U_i^\beta - U_{ij}^{*\beta}\right)\left(x_j^\alpha - x_i^\alpha\right) - \frac{2}{3}\delta^{\alpha\beta}(\overrightarrow{U_i} - \overrightarrow{U_{ij}^*})(\vec{r_j} - \vec{r_i})\right]\frac{1}{|\vec{r_j} - \vec{r_i}|}. \tag{A.4}$$

The elastic stresses are to be corrected regarding rotation of the particle as a rigid body with the rotation rate

$$\vec{\omega} = \frac{1}{2}(\nabla \times \vec{U}), \tag{A.5}$$

which is approximated as

$$\begin{aligned}
\omega_i^x &= \sum_j \frac{m_j W'_{ij}}{\rho_j h}\left[\left(U_i^z - U_{ij}^{*z}\right)(y_j - y_i) - \left(U_i^y - U_{ij}^{*y}\right)(z_j - z_i)\right]\frac{1}{|\vec{r_j} - \vec{r_i}|},\\
\omega_i^y &= \sum_j \frac{m_j W'_{ij}}{\rho_j h}\left[\left(U_i^x - U_{ij}^{*x}\right)(z_j - z_i) - \left(U_i^z - U_{ij}^{*z}\right)(x_j - x_i)\right]\frac{1}{|\vec{r_j} - \vec{r_i}|},\\
\omega_i^z &= \sum_j \frac{m_j W'_{ij}}{\rho_j h}\left[\left(U_i^y - U_{ij}^{*y}\right)(x_j - x_i) - \left(U_i^x - U_{ij}^{*x}\right)(y_j - y_i)\right]\frac{1}{|\vec{r_j} - \vec{r_i}|}.
\end{aligned} \tag{A.6}$$

The rotation rate $\vec{\omega}$ defines the orientation of the new coordinate system $x'y'z'$, frozen in the body, with respect to the old coordinate system xyz. The direction cosines $e^{\alpha'\alpha}$ of the

new eigenvectors $\vec{e^{\alpha}} = l^{\alpha'\alpha}\,\vec{e^{\alpha}}$ are described by the differential equations

$$\frac{dl^{\alpha'\alpha}}{dt} = (\vec{\omega} \times \overrightarrow{e^{\alpha'}}), \quad \alpha = x, y, z, \quad \alpha' = x', y', z', \tag{A.7}$$

and the corrected deviatoric stresses are

$$S_{\omega}^{\alpha\beta} = l^{\alpha'\alpha} l^{\beta'\beta} S_e^{\alpha'\beta'}. \tag{A.8}$$

For description of elastic, perfectly plastic flow, the Wilkins correction [18]

$$S^{\alpha\beta} = K_p S_{\omega}^{\alpha\beta} \tag{A.9}$$

is used, where the correction factor K_p according to the von Mises yield criterion is

$$K_p = \begin{cases} 1, & \text{for } f \le 2Y_0^2, \\ Y_0\sqrt{2/f}, & \text{for } f > 2Y_0^2, \end{cases} \tag{A.10}$$

and $f = 3S_{\omega}^{\alpha\beta} S_{\omega}^{\alpha\beta}$. The equation of state is taken in the Mie–Gruneisen form with the reference state defined for compression as the Hugoniot

$$P = \begin{cases} P_H + \gamma_\rho (E - E_H), & \text{for } \rho > \rho_0, \\ \gamma\rho E + K(\rho - \rho_0)/\rho_0, & \text{for } \rho \le \rho_0, \end{cases} \tag{A.11}$$

where

$$P_H = \frac{\rho_0 C_a^2 \eta}{(1 - S_a \eta)^2}, \quad E_H = \frac{P_H \eta}{2_{\rho 0}}, \quad \eta = \frac{\rho - \rho_0}{\rho}.$$

The parameters C_a and S_a are the coefficients of the Hugoniot

$$U_s = C_a + S_a U_p. \tag{A.12}$$

APPENDIX B

Algorithm for Solution of Elastic, Perfectly Plastic SPH Equations

The algorithm is composed of two major blocks. The first block is designed for computation of sums entering the right-hand parts of SPH equations. In this block, enclosed cycles with respect to i and j are used. The second block constitutes a simple cycle performing time integration of SPH equations. The computational region contains N particles of mass m_i and diameter

$$D_i = (m_i/\rho_i)^{1/3}. \tag{B.1}$$

For each basic particle, a surrounding particle is taken according to the smoothing distance

$$h = 0.5(D_i + D_j). \tag{B.2}$$

The quantities W'_{ij}, $\overrightarrow{U^*_{ij}}$, and $\overrightarrow{\sigma^*_{ij}}$ are calculated for each pair of particles. The distance between the particles,

$$|\vec{r_j} - \vec{r_i}| = \sqrt{(x_j - x_i)^2 + (y_j - y_i)^2 + (z_j - z_i)^2}, \tag{B.3}$$

is used for calculation of the smoothing kernel (47) and its derivative and the direction cosines of the axis R:

$$l^{Rx} = \frac{x_j - x_i}{|\vec{r_j} - \vec{r_i}|}, \quad l^{Ry} = \frac{y_j - y_i}{|\vec{r_j} - \vec{r_i}|}, \quad l^{Rz} = \frac{z_j - z_i}{|\vec{r_j} - \vec{r_i}|}. \tag{B.4}$$

In the smoothing kernel (47), the normalizing factor is $N = \pi h^3$.

The matrix of the direction cosines of the coordinate system RST is determined through (B.4) according to the relationship of transition between Cartesian and spherical frames of reference

$$\begin{bmatrix} l^{Rx} & l^{Ry} & l^{Rz} \\ l^{Sx} & l^{Sy} & l^{Sz} \\ l^{Tx} & l^{Ty} & l^{Tz} \end{bmatrix} = \begin{bmatrix} \cos\varphi \sin\theta & \sin\varphi \sin\theta & \cos\theta \\ \cos\varphi \cos\theta & \sin\varphi \cos\theta & -\sin\theta \\ -\sin\varphi & \cos\varphi & 0 \end{bmatrix}. \tag{B.5}$$

Transformation of vectors $\vec{U}$ and $\overrightarrow{\sigma^R}$ from coordinates x, y, z to coordinates R, S, T is given by

$$\begin{bmatrix} U^R \\ U^S \\ U^T \end{bmatrix}_k = \begin{bmatrix} l^{Rx} & l^{Ry} & l^{Rz} \\ l^{Sx} & l^{Sy} & l^{Sz} \\ l^{Tx} & l^{Ty} & l^{Tz} \end{bmatrix} \begin{bmatrix} U^x \\ U^y \\ U^z \end{bmatrix}_k, \tag{B.6}$$

$$\begin{bmatrix} \sigma^{RR} \\ \sigma^{SR} \\ \sigma^{TR} \end{bmatrix}_k = \begin{bmatrix} l^{Rx} & l^{Ry} & l^{Rz} \\ l^{Sx} & l^{Sy} & l^{Sz} \\ l^{Tx} & l^{Ty} & l^{Tz} \end{bmatrix} \begin{bmatrix} \sigma^{xR} \\ \sigma^{yR} \\ \sigma^{zR} \end{bmatrix}_k, \tag{B.7}$$

where

$$\begin{bmatrix} \sigma^{xR} \\ \sigma^{yR} \\ \sigma^{zR} \end{bmatrix}_k = \begin{bmatrix} \sigma^{xx} & \sigma^{xy} & \sigma^{xz} \\ \sigma^{yx} & \sigma^{yy} & \sigma^{yz} \\ \sigma^{zx} & \sigma^{zy} & \sigma^{zz} \end{bmatrix}_k \begin{bmatrix} l^{Rx} \\ l^{Ry} \\ l^{Rz} \end{bmatrix}, \tag{B.8}$$

and $k = i, j$. The intermediate quantities $\overrightarrow{U^*_{ij}}$ and $\overrightarrow{\sigma^{*R}_{ij}}$ are computed according to (23)–(28) and then retransformed to coordinates x, y, z by

$$\begin{bmatrix} U^{*x}_{ij} \\ U^{*y}_{ij} \\ U^{*z}_{ij} \end{bmatrix} = \begin{bmatrix} l^{Rx} & l^{Ry} & l^{Rz} \\ l^{Sx} & l^{Sy} & l^{Sz} \\ l^{Tx} & l^{Ty} & l^{Tz} \end{bmatrix} \begin{bmatrix} U^{*R}_{ij} \\ U^{*S}_{ij} \\ U^{*T}_{ij} \end{bmatrix}, \tag{B.9}$$

$$\begin{bmatrix} \sigma^{*xR}_{ij} \\ \sigma^{*yR}_{ij} \\ \sigma^{*zR}_{ij} \end{bmatrix} = \begin{bmatrix} l^{Rx} & l^{Ry} & l^{Rz} \\ l^{Sx} & l^{Sy} & l^{Sz} \\ l^{Tx} & l^{Ty} & l^{Tz} \end{bmatrix} \begin{bmatrix} \sigma^{*RR}_{ij} \\ \sigma^{*SR}_{ij} \\ \sigma^{*TR}_{ij} \end{bmatrix}. \tag{B.10}$$

The next step is computation of the right parts of SPH equations (14), (31), (32), (A.4), and (A.6).

The second block of the algorithm performs integration of equations of momentum and energy conservation (20) and (21) and constitutive equation (A.6) by means of explicit time integration scheme

$$f_i^{n+1} = f_i^n + F_i^n\left(\vec{r}_i^{\,n}\right)\Delta t, \tag{B.11}$$

where $f_i = \overrightarrow{U_i}$, E_i, $S_{ei}^{\alpha\beta}$, and F_i is the right part of (31), (32), and (A.4), respectively.

The continuity equation (14) is integrated as

$$\rho_i^{n+1} = \rho_i^n \left(\frac{2 - \dot{\varepsilon}_i \Delta t}{2 + \dot{\varepsilon}_i \Delta t}\right)^n, \tag{B.12}$$

where

$$\dot{\varepsilon}_i = -2\sum_j \frac{m_j W'_{ij}}{\rho_j h}\left(U_i^R - U_{ij}^{*R}\right). \tag{B.13}$$

Since (A.7) is integrated for each time step Δt^n at identical initial conditions $l^{\alpha'\alpha} = \delta^{\alpha'\alpha}(\alpha = x, y, z, \alpha' = x', y', z')$, we have the following solution for the matrix of the direction cosines:

$$\begin{bmatrix} l^{x'x} & l^{x'y} & l^{x'z} \\ l^{y'x} & l^{y'y} & l^{y'z} \\ l^{z'x} & l^{z'y} & l^{z'z} \end{bmatrix} = \begin{bmatrix} 1 & \omega_z \Delta t & -\omega_y \Delta t \\ -\omega_z \Delta t & 1 & \omega_x \Delta t \\ \omega_y \Delta t & -\omega_x \Delta t & 1 \end{bmatrix}. \tag{B.14}$$

The correction of the deviatoric stress tensor needed because of the rigid rotation is made by matrix multiplication:

$$\left[S_\omega^{\alpha\beta}\right] = [l^{\alpha'\alpha}]\left[S_e^{\alpha'\beta'}\right][l^{\beta'\beta}]^T. \tag{B.15}$$

The procedure (B.15) is performed by the functions MATMUL and TRANSPOSE integrated in FORTRAN 90. For the ideally plastic medium, the corrections (A.9) and (A.10) are used. The pressure is computed by (A.11). The stress tensor is now obtained from (A.1).

Finally, the new position of the particle is calculated as

$$\overrightarrow{r_i^{n+1}} = \vec{r}_i^{\,n} + \frac{1}{2}\left(\overrightarrow{U_i^{n+1}} + \overrightarrow{U_i^n}\right)\Delta t^n. \tag{B.16}$$

The time step is computed according to the Courant criterion

$$\Delta t = \min\left(\frac{\beta D_i}{\sqrt{C_i^2 + \left(4 D_i \dot{\varepsilon}_i^{\alpha\alpha}\right)^2}}\right). \tag{B.17}$$

Multiple computations demonstrated the stable solution to be for $\beta \le 0.8$.

REFERENCES

1. R. A. Gingold and J. J. Monaghan, Kernel estimates as a basis for general particle methods in hydrodynamics, *J. Comput. Phys.* **46**, 429 (1982).
2. J. J. Monaghan, On the problem of penetration in particle methods, *J. Comput. Phys.* **82**, 1 (1989).
3. G. R. Jonson, E. H. Petersen, and R. A. Stryk, incorporation of an SPH option into the EPIC code for a wide range of high velocity impact computations, *Int. J. Impact Eng.* **14**, 385 (1993).
4. C. A. Wingate and H. N. Fisher, *Strength Modeling in SPHC*, Los Alamos National Laboratory Report LA-UR-93-3942 (1993).
5. L. D. Libersky, P. W. Randles, T. C. Carney, and D. L. Dickinson, Recent improvements in SPH modeling of hypervelocity impact, *Int. J. Impact Eng.* **7**, 525 (1997).
6. S. K. Godunov, Difference method of numerical computation of discontinuous solution of hydrodynamic equations, *Math. Sb.* **47**, 271 (1959), in Russian.
7. J. J. Monaghan, SPH and Riemann solvers, *J. Comput. Phys.* **136**, 298 (1997).
8. A. N. Parshikov, Application of a solution of the Riemann problem to the SPH method, *Comput. Math. Math. Phys.* **39**, 1173 (1999).
9. A. N. Parshikov, S. A. Medin, I. I. Loukashenko, and V. A. Milekhin, Improvements in SPH method by means of interparticle contact algorithm and analysis of perforation tests at moderate projectile velocities, *Int. J. Impact Eng.* **24**, 779 (2000).
10. P. W. Cleary and J. J. Monaghan, Conduction modeling using smoothed particle hydrodynamics, *J. Comput. Phys.* **148**, 227 (1999).
11. J. J. Monaghan, SPH without a tensile instability, *J. Comput. Phys.* **159**, 290 (2000).
12. H. S. Carlslaw and J. C. Jager, *Conduction of Heat in Solid* (Oxford Univ. Press, London, 1965).
13. J. K. Dukowicz, A general, non-iterative Riemann solver for Godunov's method, *J. Comput. Phys.* **61**, 119 (1985).
14. H. Lamb, *Hydrodynamics*, 6th ed. (Cambridge Univ. Press, Cambridge, UK, 1932).
15. S. P. Timoshenko and J. N. Goodier, *Theory of Elasticity* (McGraw-Hill, New York, 1970).
16. V. V. Bashurov, G. V. Bebenin, G. V. Belov, Y. N. Bukharev, V. I. Zhukov, A. G. Ioilev, N. V. Lapichev, A. L. Mikhailov, G. S. Smirnov, Y. A. Fateev, and G. P. Schlyapnikov, Experimental modeling and numerical simulation of high- and hypervelocity space debris impact to spacecraft shield protection, *Int. J. Impact Eng.* **20**, 69 (1997).
17. P. H. L. Groenenboom, Numerical simulation of 2D and 3D hypervelocity impact using the SPH option in RAM-SHOCK™, *Int. J. Impact Eng.* **20**, 309 (1997).
18. M. L. Wilkins, Computation of elastic–plastic flow, in *Methods of Computational Physics*, edited by B. Alder, S. Fernbach, and M. Rotenberg (Academic Press, New York, 1964), Vol. 3.